# Time-resolved imaging of magnetization dynamics in double nanocontact spin torque vortex oscillator devices

Erick Burgos-Parra,[1,*] Paul S. Keatley,[1] Sohrab Sani,[2] Phillip Durrenfeld,[3] Johan Åkerman,[2,3] and Robert J. Hicken[1]

[1]*Department of Physics and Astronomy, University of Exeter, Exeter EX4 4QL, United Kingdom*

[2]*Department of Materials and Nanophysics, School of Engineering Sciences, KTH Royal Institute of Technology, 164 40 Kista, Sweden*

[3]*Department of Physics, University of Gothenburg, 412 96 Gothenburg, Sweden*

(Received 11 February 2019; revised manuscript received 27 August 2019; published 31 October 2019)

Double nanocontact (NC) spin transfer vortex oscillator devices, in which NCs of 100-nm diameter have center-to-center separation ranging from 200 to 1100 nm, have been studied by means of electrical measurements and time-resolved scanning Kerr microscopy (TRSKM). The NCs were positioned close to the edge of the top electrical contact so that the magnetization dynamics of the adjacent region could be probed optically. The electrical measurements showed different ranges of frequency operation for devices with different NC separations. For 900-nm NC separation, TRSKM showed magnetic contrast consistent with the formation of a magnetic vortex at each NC, while for 200-nm NC separation a lack of magnetic contrast near the NC region suggests that the magnetization dynamics occur closer to the NC and underneath the top contact. TRSKM also reveals the presence of additional localized dynamical features far from the NCs, which are not seen by electrical measurements; has not been reported previously for double NCs with different separations; and provides insight into how the dynamic state of the phase-locked oscillators is established and stabilized.

DOI: 10.1103/PhysRevB.100.134439

## I. INTRODUCTION

Since the prediction [1,2] and experimental observation [3,4] of spin transfer torque (STT), great efforts have been made to deliver large-scale integration of devices that exploit its unique features [5]. STT is exerted upon the magnetization of a magnetic material when it absorbs the angular momentum carried by a spin-polarized current [6]. Typically, STT is observed within spin-valve structures where it can either suppress the magnetic damping in the free layer (FL), generate a persistent precession of the magnetization vector, or induce full reversal of the magnetization [1,2,7]. Within a spin torque oscillator (STO) [3,8–11], a steady precession combines with the magnetoresistance of the device structure to generate a microwave voltage signal. STOs promise to be a cornerstone for the development of future technologies such as magnetic memories [12,13], microwave nanoemitters [14,15], and neuromorphic computing [16], among others. Multiple designs have been studied in the form of mechanical point contacts [3,17], lithographically defined nanopillars [18–23], and nanocontacts (NCs) [24–31] in order to resolve two critical bottleneck issues for the realization of STO devices: The phase stability and low power emission [24].

Placement of a NC on top of the FL of a spin valve is a promising design due to its high quality factor and the ease with which it can be combined with conventional semiconductor technology.

When the magnetization of the free and fixed layers lies in the plane of the film, the Oersted field produced by the DC current in the NC leads to the formation of a vortex in the FL, while the STT sustains vortex gyration. In this case the microwave emission of the NC-STO is driven by the gyrotropic motion of a vortex instead of magnetization precession. Vortex-based devices exhibit multioctave frequency tunability and higher power output than precession-based oscillators [25,26,32,33]. However, the output power is still too low, and the line width is too broad for technological applications [34]. Phase-locked spin torque vortex oscillators (STVOs) formed from multiple NCs on a spin-valve mesa are anticipated to exhibit enhanced microwave power and phase stability compared to single NC oscillators [35–39], providing a solution to the drawbacks of the NC-STO in the low-frequency regime (100 MHZ to 1 GHz).

While the microwave emission due to the vortex gyration beneath the NC can be characterized by electrical measurements, the magnetization dynamics beyond the perimeter of the NC cannot. Knowledge of the spatiotemporal character of such dynamics is an essential prerequisite for successful mutual phase locking of STVOs. In this work STVO devices with pairs of NCs of 100-nm diameter and center-to-center separation $D = 200$ to 1100 nm are studied by a combination of electrical measurements and time-resolved scanning Kerr microscopy (TRSKM) [40–43]. Microwave emission is studied for the full range of $D$ values, and the associated magnetization dynamics of the FL has been imaged with TRSKM for $D = 200$, 300, and 900 nm. It will be shown that vortices gyrate about the individual NCs for large $D$ values and are visible outside the footprint of the top contact, while for small $D$ values the dynamics are more tightly confined

*erick.burgos@cnrs-thales.fr

 

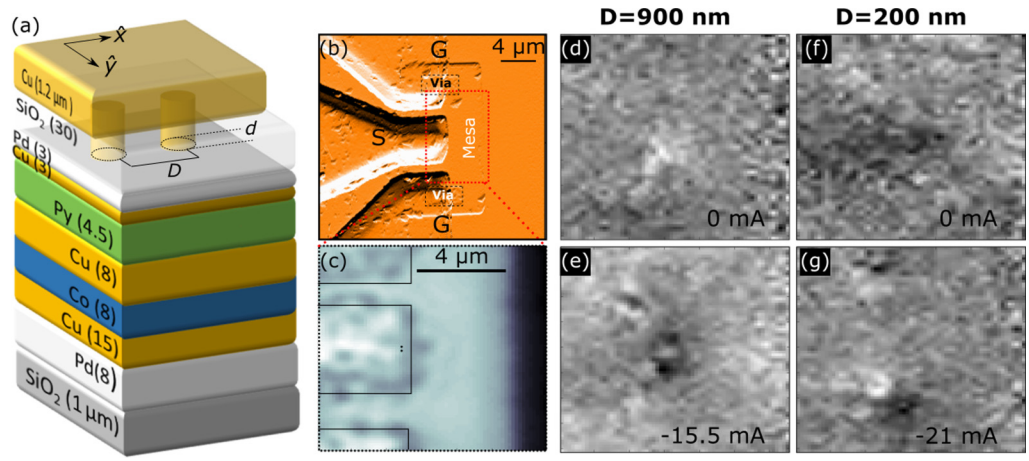


FIG. 1. (a) Schematic of the spin valve mesa stack (layer thicknesses in nanometers) with NCs of diameter $d$ and separation $D$. Co(8) and Py(4.5) are the reference and free layers, respectively. The DC current is injected via a CPW and two NCs of 100-nm diameter. (b) CPW geometry with ground (G) and signal (S) electrical contacts. (c) Reflectivity image of a typical device corresponding to the section enclosed in the dashed square in (b). The dots close to the short edge of the signal contact in (c) show the estimated position of the NCs. For a device with $D = 900$ nm, the change in the magnetization in the $\hat{\mathbf{x}}$ direction in the presence of a $-10$-dBm rf current is shown at (d) 0 and (e) $-15.5$ mA DC current. Similarly, for $D = 200$ nm, the change in the magnetization in the $\hat{\mathbf{x}}$ direction is shown for (f) 0 and (g) $-21$ mA DC current.

to the immediate vicinity of the NCs. Additional dynamic structures appear at the corners of the top contact that may result from the presence of antivortices.

## II. EXPERIMENTAL METHOD

### A. Sample details

All STVOs studied in the present work were formed on $16 \times 8$ $\mu$m$^2$ spin-valve mesas that comprised a Si/$SiO_2$ (thermally oxidized, 1 $\mu$m) substrate supporting a Pd(8)/Cu(15)/Co(8)/Cu(7)/$Ni_{81}Fe_{19}$(4.5)/Cu(3)/Pd(3) (thickness in nanometers) stack, as shown in Fig. 1(a). Co and Cu(7) are the reference (RL) and spacer (SL) layers, while the NiFe layer, an alloy known as permalloy (Py), forms the FL of the STO in which magnetization dynamics associated with nucleation and gyration are observed. A $SiO_2$(30) layer was deposited on top of the FL. Pairs of NCs of 100-nm nominal diameter and center-to-center separation $D$ ranging from 200 to 1100 nm were then defined using electron-beam lithography, followed by reactive ion etching. Cu NCs were formed by the deposition of a Cu(1200)/Au(20) bilayer that also formed a coplanar wave guide that had a characteristic impedance of 50 Ω for microwave electrical contacts. A detailed explanation of the fabrication process can be found in Ref. [42].

### B. Electrical measurements

Electrical transport measurements were performed to probe the frequency of microwave emission stimulated by a DC electric current $I_{DC}$. The current was supplied to the STVO via the coplanar wave guide (CPW) connected to a bias tee that allowed the emitted microwave current to be separated from $I_{DC}$ and directed into a spectrum analyzer. Negative DC current is defined as electrons moving from the free layer to the reference layer. We observed auto-oscillations only for negative current, ruling out thermal excitation of the observed auto-oscillations. To ensure that any initial nonuniform magnetic structure within the mesa was removed, an in-plane magnetic field of ∼20 mT was first applied parallel to the long edge of the mesa. The field was then reduced to a value of 3 mT before the $I_{DC}$ was applied. The $I_{DC}$ was swept from $-40$ to 0 mA to ensure the nucleation of the magnetic vortices due to the high local Oersted field in the NC area. In order to phase lock the magnetization dynamics of the STVOs for time-resolved measurements an additional microwave current ($I_{RF}$) was injected using a microwave synthesizer and a circulator. The amplitude of the $I_{RF}$ current was nominally $-10$ dBm, which is typically $\sim 0.1 I_{DC}$ in the middle of the locking range.

### C. Time-resolved scanning Kerr microscopy

Time-resolved Kerr images were acquired using laser pulses from a Ti:sapphire oscillator that had ∼100-fs duration, 80-MHz repetition rate, and 800-nm wavelength. The spatial resolution was previously determined to be ∼500 nm using the knife edge technique [44,45]. In order to perform stroboscopic measurements, the laser and the microwave synthesizer used to inject $I_{RF}$ into the STVO were phase locked to an 80-MHz master clock. The frequency of $I_{RF}$ was therefore required to be an integer multiple of 80 MHz. In the present work, the STVO was locked at a frequency of 160 MHz for time-resolved (TR) measurements. The phase of $I_{RF}$ was modulated through 180° at ∼3 kHz so that the change in the magnetization could be recorded by lock-in detection. Each image was acquired at a fixed phase of the injected rf current, and the longitudinal and polar magneto-optical Kerr effects were used to recover the three spatial components of the dynamic magnetization simultaneously. The coordinate system is defined in Fig. 1(a), where the $\hat{x}$ direction lies along the long edge of the mesa and the $\hat{y}$ direction is along the short edge. All TRSKM measurements were performed with a 3-mT bias field applied parallel to the $x$ axis. A

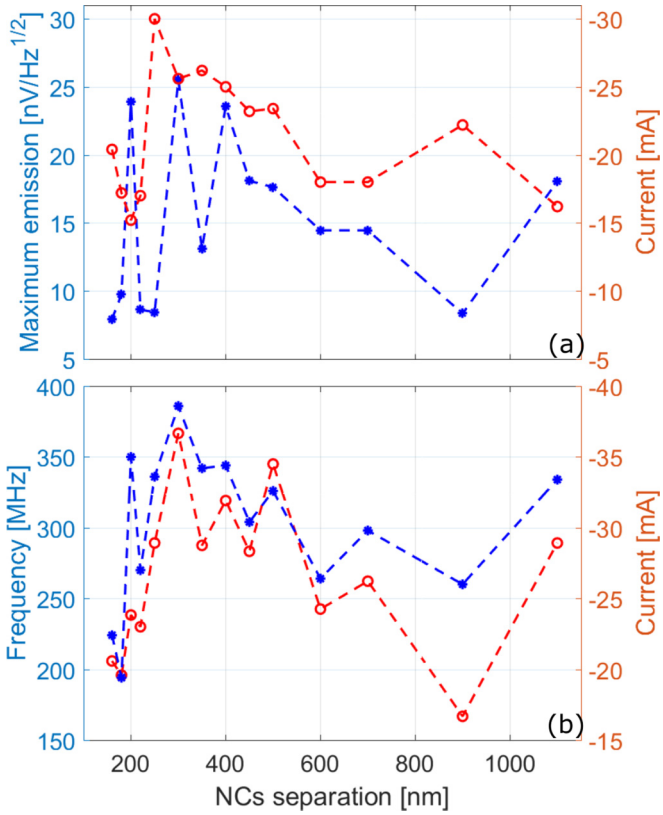


FIG. 2. (a) Dependence of peak microwave emission (blue solid circles) and the current (open red circles) at which peak emission was observed upon NC separation. (b) Frequency (blue solid circles) at which an emission of greater than $5\,\mathrm{nV}/\sqrt{\mathrm{Hz}}$ was observed as $I_{\mathrm{DC}}$ was reduced from $-40$ to 0 mA and the current (red open circles) value at which this occurred.

more detailed explanation of the experimental technique was provided previously [42,43,46].

## III. RESULTS

Electrical measurements were performed at remanent field ($\leqslant$0.5 mT) upon devices with values of $D$ ranging from 160 to 1100 nm. Figure 2(a) shows the peak microwave emission (blue solid circles) and the current needed to observe such emission (red open circles) for different $D$ values. The peak emission varies nonmonotonically from $7.9\,\mathrm{nV}/\sqrt{\mathrm{Hz}}$ for $D =$ 160 nm to $25.5\,\mathrm{nV}/\sqrt{\mathrm{Hz}}$ for $D = 300$ nm. From these electrical measurements alone it is unclear why different current values of 15 and 25 mA are required to achieve emissions with a similar amplitude at $D = 200$ nm and $D = 300$ nm, respectively. One speculative explanation could be that a single vortex gyrates about both NCs when $D = 200$ nm, so that the magnetization beneath each NC rotates in phase. In contrast, when $D = 300$ nm, if a separate vortex is localized at each NC, then a larger current may be required to phase lock their dynamic response in the presence of their respective dynamic dipolar and exchange fields that may act to introduce a phase difference [44,47].

Figure 2(b) shows the frequency at which the amplitude of emission exceeds $\geqslant 5\,\mathrm{nV}/\sqrt{\mathrm{Hz}}$ (blue solid circles) as $I_{\mathrm{DC}}$ is swept from $-40$ to 0 mA and the value of the current (red open circles) at which this occurs. It is interesting to note that, in general, the nonmonotonic variation of onset frequency follows that of the current at which the onset is observed. This is useful for applications since it shows the optimum device geometry for operation at the lowest current. For example, when $D = 200$ nm, it can be seen that the onset of auto-oscillation occurs at a relatively small current of $\sim$24 mA compared to $\sim$37 mA for $D = 300$ nm. At the same time Fig. 2(a) shows that the peak emission at $D = 200$ nm requires the minimum current. The larger current required at $D = 300$ nm may indicate an energetically unfavorable transition from small to large NC separations, which support a single vortex and multiple vortices, respectively.

From this initial screening, the devices chosen for TRSKM measurements were those with $D = 200$ and 300 nm, due to their large peak emission and higher frequency of operation but quite different current requirements and number of modes, and $D = 900$ nm, on account of its small peak emission and lower frequency of operation, which may result from vortices gyrating on each NC with a significant phase difference. This choice of devices allows TRSKM to explore the suggestion that single and multiple vortices form at pairs of NCs with small and large values of $D$, respectively.

Figures 3(a) and 3(b) show the voltage spectral density (VSD) of the emission from devices with $D = 200$ and 900 nm, respectively, with an external field of 3 mT applied parallel to the $\hat{x}$ axis. The value of $I_{\mathrm{DC}}$ was swept from the largest negative value to zero. For $D = 200$ nm, a single fundamental mode is observed for large negative $I_{\mathrm{DC}}$, which splits at $I_{\mathrm{DC}} = -15.2$ mA before disappearing at $I_{\mathrm{DC}} = -10.2$ mA. The inset in Fig. 3(a) shows the VSD for the same device with zero external field, where a single broad mode splits into two modes at $I_{\mathrm{DC}} \sim -25.5$ mA. The lower-frequency mode vanishes at $I_{\mathrm{DC}} \sim -15$ mA, while the higher-frequency mode persists until $I_{\mathrm{DC}} \sim -3.8$ mA. On the other hand, for $D =$ 900 nm, again with 3-mT external field applied, two modes are observed that coexist between $I_{\mathrm{DC}} \sim -24.5$ and $-17.6$ mA. Thereafter, only the higher-frequency mode is observed until it disappears at $I_{\mathrm{DC}} \sim -7.6$ mA. The inset in Fig. 3(b) shows the VSD of the same device for zero external field. In this case, two modes coexist until $I_{\mathrm{DC}} \sim -7$ mA, while the remaining mode vanishes at $-5$ mA.

The changes in mode frequency observed as $|I_{\mathrm{DC}}|$ is decreased are associated with a change in the trajectory of vortex precession, which results from a reduction of the Oersted field that, in turn, modifies the equilibrium magnetization within the vicinity of the NC [48]. In a similar way, the mode character also depends upon the value of the external field [42]. It is interesting to note that, when an external field is applied, for $I_{\mathrm{DC}} = -21$ mA and $D = 200$ nm, the two modes observed at zero field turn into a single mode with lower frequency, higher amplitude, and smaller linewidth, as can be seen in Fig. 3(e). This is consistent with the formation of a single vortex that gyrates about both NCs [49].

However, for a device with $D = 900$ nm and $I_{\mathrm{DC}} =$ $-12.9$ mA, there are again two modes at zero field that turn into a single mode when the field is applied. At remanence the emission hops between single- and multimode states when the magnitude of the current is reduced from approximately 16

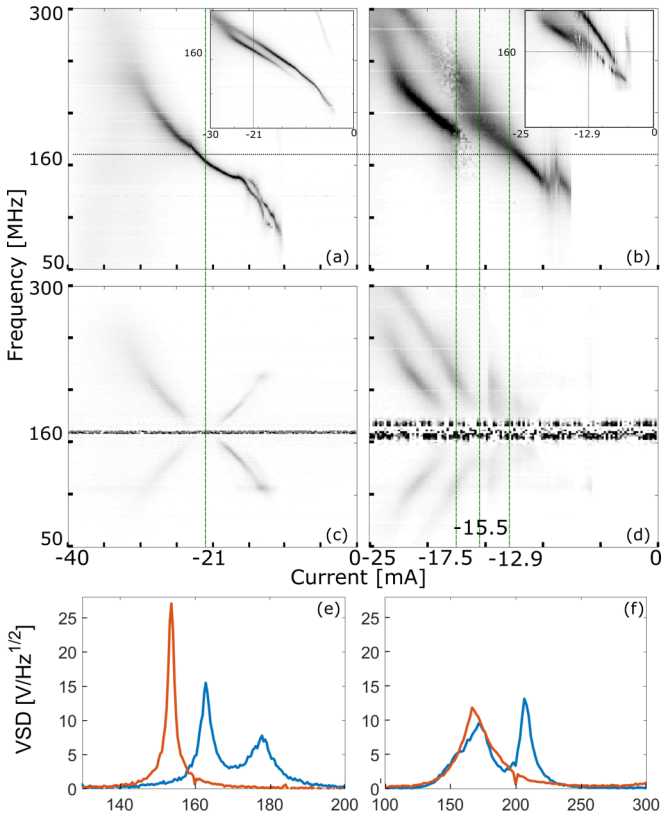


FIG. 3. Voltage spectrum density (VSD) of the emission from devices with (a) $D = 200$ nm and (b) $D = 900$ nm, with an external magnetic field of $\sim$3 mT applied parallel to the $x$ axis. The inset figures show similar measurements made in zero external field. VSD of emission from devices with (c) $D = 200$ nm and (d) $D = 900$ nm when the vortex gyration frequency is injection locked at 160 MHz. The green dashed lines indicate the current values for which TRSKM images were acquired. Frequency dependence of VSD at (e) $I_{DC} = -21$ mA for $D = 200$ nm and (f) $I_{DC} = -12.9$ mA for $D = 900$ nm for $I_{RF} = 0$, zero applied field (blue curve), and 3 mT applied parallel to the $x$ axis (red curve).

to 8 mA. This suggests either that the lower-frequency mode corresponds to two vortices oscillating with a substantial and variable phase difference such that when they oscillate out of phase, the emission vanishes or that the system is hopping between a single- and multivortex state [49]. However, it is not possible to determine the dynamic magnetization configuration of the sample from the electrical measurements alone.

Figures 1(d)–1(g) show the $x$ component of the change in magnetization observed in TRSKM measurements for devices with $D = 200$ and 900 nm. The $x$ component has been chosen because it is easier to identify the main features of the dynamics, but all three components of the dynamic magnetization, for all devices and all values of the phase of the injected microwave current, can be found in the Supplemental Material [50], in addition to measurements on a device with $D = 300$ nm. There are clear differences between the images acquired for finite [Figs. 1(e) and 1(g)] and zero [Figs. 1(d) and 1(f)] $I_{DC}$ values. In both cases the value of $I_{DC}$ has been chosen to yield emission at 160 MHz. The images demonstrate that the dynamics observed in Figs. 1(e) and 1(g) are in response to STT delivered by $I_{DC}$ and not excited by the $I_{RF}$ Oersted field alone, as confirmed in [42].

Figure 4(a) shows TRSKM images obtained from the device with $D = 200$ nm and with $I_{DC} = -21$ mA. Two regions of strong contrast may be seen close to the corners of the signal contact of the CPW [regions B and C in Fig. 4(b)]. One possible explanation for the position of these dynamics is that antivortices (formed at the same time as vortex nucleation) have drifted away from the NC and have become pinned close to the corners of the top signal contact. Similar displacement of antivortices far from the NC have been observed in micromagnetic simulations for single NC devices [42,51]. The antivortices then oscillate in response to the rf field and/or dynamic dipolar interaction with vortices close to the NCs. Such dynamics have also been observed in single NC devices, and further studies with enhanced spatial resolution are required to elucidate their origin [42,46]. The electrical measurements shown in Fig. 3 indicate that when the DC current is applied with zero external magnetic field, a magnetic vortex is created within the vicinity of each NC for $D = 200$ and 900 nm, and each vortex has its own characteristic frequency of gyration corresponding to the two observed modes [insets in Figs. 3(a) and 3(b)]. However, when an external field of 3 mT is applied along the short edge of the top contact, only a single mode is observed in electrical measurements when $s = 200$ nm [Fig. 3(a)]. In this case either the gyration of one vortex is favored, while the other is expelled outside of the NC and no longer contributes to the electrical signal, or one of the vortices has been annihilated by the antivortex formed during the nucleation process. It was not possible to directly image the dynamics associated with this single mode when $D = 200$ nm. The clear observation of the single mode in the electrical measurements means that the vortex is strongly localized in the vicinity of the NCs, and therefore, its associated dynamics do not extend beyond the edge of the top contact for optical detection. The observed change in electrical behavior with the applied magnetic field is most likely due to one vortex remaining near the NC, perhaps with the trajectory of its core enclosing both NCs. This would yield the observed decrease in the observed frequency of gyration and the presence of only a single emission line [49].

For the device with $D = 900$ nm, there are three current values of interest when the microwave emission is locked at 160 MHz, as shown in Fig. 3(d). For $I_{DC} = -12.9$ mA [Fig. 4(c)], the dynamics outside the short edge of the top contact [region A in Fig. 4(b)] are weak, inhomogeneous, and not indicative of stable vortex gyration observed previously [42]. There is also a subtle change in contrast at the top corner of the top contact [Fig. 4(c) at 0°, see arrow]. The amplitude of the Kerr signal of this region increases as $I_{DC}$ is changed from $-12.9$ to $-15.5$ mA [Fig. 4(d)] and then to $-17.5$ mA [Fig. 4(e)], while along the short edge of the top contact pad localized dynamics emerge outside the vicinity of the NC. For these latter $I_{DC}$ values, the observed contrast along the short edge is consistent with the formation of a vortex on each NC [42]. The similar intensities of the two regions of localized dynamics at $-17.5$ mA are consistent with the interpretation that the pair of vortices gyrates in phase. At $-15.5$ mA a difference in the size and intensity of these two regions indicates that the vortices oscillate with a phase

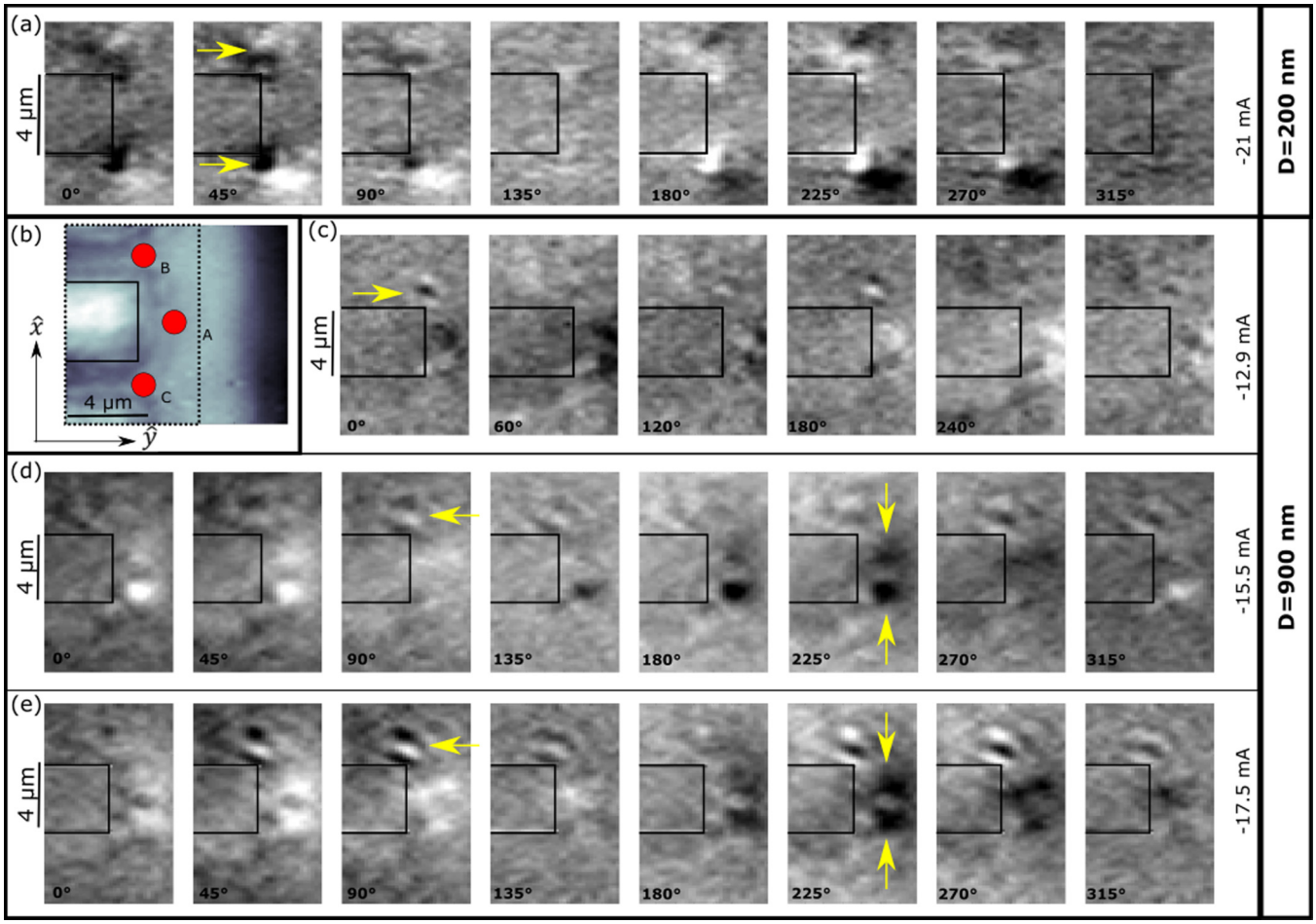


FIG. 4. (a) TRSKM images acquired for different values of the phase of $I_{RF}$, with $I_{DC} = -21$ mA and a 30-Oe bias field applied parallel to the $x$ axis, for a device with $D = 200$ nm. (b) Full reflectivity image of a typical device, where the dashed line shows the region studied in TRSKM measurements, and the red dots show regions of specific interest, with A being the region close to the NCs and B and C being close to the corners of the top contact. Similar measurements to those made in (a) were made upon a device with $D = 900$ nm for $I_{DC}$ values of (c) $-12.9$ mA, (d) $-15.5$ mA, and (e) $-17.5$ mA. All images show the change in the $x$ component of magnetization when the STVO is injection locked at a frequency of 160 MHz. The gray scale represents the output voltage of the optical bridge detector. Each pixel in each image was normalized to its corresponding pixel in the reflectivity image for each phase. The reflectivity image was first normalized to a region in the mesa layer far away from the top signal contact. Yellow arrows point to the spatial position of a significant change in contrast associated with magnetic structures such as vortices on antivortices.

difference. Note that this will not appear as an out-of-phase mode because both NCs are injection locked by the same rf current, which forces a similar phase of the gyration. Instead, the presence of dynamic interaction between two oscillators in the presence of the same rf source will introduce a phase difference in a way similar to that observed in Refs. [44,52].

At $-17.5$ mA the enhanced contrast of the localized dynamics is consistent with enhanced STT due to the larger value of $I_{DC}$ [42]. The enhanced STT will lead to a larger radius of gyration. The contrast of the localized regions will also be enhanced when their area becomes comparable to or larger than the optical spot size, so that the contrast is no longer suppressed by the spatial resolution, which may be the case at $-12.9$ mA.

It is expected that gyration of the vortices about the NCs is driven solely by the STT. However, the magnetic structures localized at the corners of the top contact are also observed to oscillate, even though no STT is expected to act upon this region. It was also observed that there is a difference in the phase of oscillation between the dynamics near the NC and those at the corners of the top contact, as can be seen by comparing regions A and B in Figs. 4(c)–4(e). Previously, it was determined that such a phase difference exists between dynamics driven by STT and those driven by the rf Oersted field [42]. Since the dynamic features at the corners of the contact pad are not observed when $I_{DC} = 0$, we conclude that they are either antivortices or additional vortices that formed within the free layer in the process of vortex formation by the DC Oersted field, which then oscillate due to the rf Oersted field.

It is interesting to note the number of modes observed in electrical measurements and the number of dynamic features far from the NC. When $D = 900$ nm, it is clear from the Kerr images that dynamics associated with a vortex gyrating are observed close to each NC [Figs. 4(d) and 4(e), arrows at 225°]. At the same time there is a single dynamic feature

pinned at the top corner of the center contact pad [Figs. 4(d) and 4(e), arrows at 90°]. Previously, we ascribed this feature to an antivortex, in accordance with micromagnetic simulations [51]. On the other hand, when $D = 200$ nm, two dynamic features are observed at the top and bottom corners of the contact pad [Fig. 4(a), arrows at 45°]. Since a single mode was observed in the electrical measurements, this suggests that one of the vortices has been expelled from the NC region and has become trapped in the electrostatic pinning potential of the top contact pad. Previous micromagnetic simulations of a single NC showed that a vortex expelled from the NC can survive outside the NC provided that its paired antivortex also remains in the film [42]. While the magnetic character of the dynamic features cannot be determined from Fig. 4(a), the presence of two features in comparison to the single feature in the device with $D = 900$ nm supports the interpretation of an expelled vortex. This is of particular importance when considering the arrangement of vortices and antivortices in continuous films for dynamic coupling of more than two NCs, such as that described in Ref. [35].

## IV. SUMMARY

In summary, combined electrical and time-resolved scanning Kerr microscopy measurements have been performed on double NC STVOs. Time-resolved images acquired for devices with center-to-center NC separation of $D = 200$ and 900 nm have been presented. The electrical measurements are richly featured, often exhibiting multiple modes and their harmonics. The frequency, output power, and associated values of $I_{DC}$ all showed nonmonotonic variation as the NC separation was reduced.

TR Kerr images acquired from the two selected devices showed spatial contrast of very different character. For $D = 900$ nm, localized regions of magnetization dynamics were observed close to each NC, with each region having spatial character similar to that found within single NC devices, suggesting that a separate vortex had formed at each NC [41,42]. However, for a pair of NCs with 200-nm separation, no dynamics were observed in the region close to the NCs. At the same time, large-amplitude dynamics were also observed at a distance of some microns from the NCs. In accordance with the number of modes observed in electrical measurements we speculate that these dynamics are due to the oscillation of vortices and/or antivortices that are pushed away from the NCs, pinned by stray DC electromagnetic fields from the top signal contact, and then excited by the stray rf Oersted field.

The dynamics at the corners of the top electrical contact are observed only when a DC current is applied, which results in the nucleation of a vortex-antivortex pair. This rules out the excitation of the FL film in response to the RF Oersted field associated with the microwave current. Such excitation is not expected since the spin wave spectrum of the film has a frequency of 1–10 GHz and should not be readily excited at 160 MHz. At the same time the spin torque excitation at the position of these corners is expected to be weak. This suggests that the dynamics near the NCs may be linked to the dynamics at the corners of the top contact through dynamic dipolar interactions or, indeed, through interactions within the film for particular equilibrium states in the presence of $I_{DC}$ [46]. However, to advance the understanding of these dynamics, further experiments and simulations are needed. An improved understanding of the interaction of pairs of NC STVOs is crucial for the realization of networks of phase-locked NC STVOs that share common magnetic layers.

## ACKNOWLEDGMENTS

We acknowledge financial support from the Engineering and Physical Sciences Research Council (EPSRC) of the United Kingdom via the EPSRC Centre for Doctoral Training in Metamaterials (Grant No. EP/L015331/1) and Grant No. EP/P008550/1 and to The Ministry of Education, Chile and Commission for Scientific and Technological Research (CONICYT) through grant BCH 72150531 has granted financial support to the PhD student during this research.

[1] J. Slonczewski, J. Magn. Magn. Mater. **159**, L1 (1996).
[2] L. Berger, Phys. Rev. B **54**, 9353 (1996).
[3] M. Tsoi, A. G. M. Jansen, J. Bass, W.-C. Chiang, M. Seck, V. Tsoi, and P. Wyder, Phys. Rev. Lett. **80**, 4281 (1998).
[4] E. B. Myers, D. C. Ralph, J. A. Katine, R. N. Louie, and R. A. Buhrman, Science **285**, 867 (1999).
[5] J. Katine and E. E. Fullerton, J. Magn. Magn. Mater. **320**, 1217 (2008).
[6] M. D. Stiles and J. Miltat, in *Spin Dynamics in Confined Magnetic Structures III*, edited by B. Hillebrands and A. Thiaville (Springer, Berlin, 2006), pp. 225–308.
[7] I. N. Krivorotov, N. C. Emley, J. C. Sankey, S. I. Kiselev, D. C. Ralph, and R. A. Buhrman, Science **307**, 228 (2005).
[8] M. Tsol, A. G. Jansen, J. Bass, W. C. Chlang, V. Tsol, and P. Wyder, Nature (London) **406**, 46 (2000).
[9] S. I. Kiselev, J. C. Sankey, I. N. Krivorotov, N. C. Emley, R. J. Schoelkopf, R. A. Buhrman, and D. C. Ralph, Nature (London) **425**, 380 (2003).
[10] W. H. Rippard, M. R. Pufall, S. Kaka, S. E. Russek, and T. J. Silva, Phys. Rev. Lett. **92**, 027201 (2004).
[11] J.-V. Kim, Solid State Physics **63**, 217 (2012).
[12] J. Åkerman, Science **308**, 508 (2005).
[13] B. N. Engel, J. Akerman, B. Butcher, R. W. Dave, M. DeHerrera, M. Durlam, G. Grynkewich, J. Janesky, S. V. Pietambaram, N. D. Rizzo, J. M. Slaughter, K. Smith, J. J. Sun, and S. Tehrani, IEEE Trans. Magn. **41**, 132 (2005).
[14] P. Villard, U. Ebels, D. Houssameddine, J. Katine, D. Mauri, B. Delaet, P. Vincent, M. C. Cyrille, B. Viala, J. P. Michel, J. Prouvee, and F. Badets, IEEE J. Solid-State Circuits **45**, 214 (2010).
[15] T. Chen, P. Dürrenfeld, S. Rodriguez, J. Åkerman, and A. Rusu, Microwave Opt. Technol. Lett. **56**, 2092 (2014).
[16] J. Torrejon, M. Riou, F. A. Araujo, S. Tsunegi, G. Khalsa, D. Querlioz, P. Bortolotti, V. Cros, K. Yakushiji, A. Fukushima, H. Kubota, S. Yuasa, M. D. Stiles, and J. Grollier, Nature (London) **547**, 428 (2017).

[17] Y. Ji, C. L. Chien, and M. D. Stiles, Phys. Rev. Lett. **90**, 106601 (2003).

[18] J. A. Katine, F. J. Albert, R. A. Buhrman, E. B. Myers, and D. C. Ralph, Phys. Rev. Lett. **84**, 3149 (2000).

[19] J. Grollier, V. Cros, H. Jaffrès, A. Hamzic, J. M. George, G. Faini, J. Ben Youssef, H. Le Gall, and A. Fert, Phys. Rev. B **67**, 174402 (2003).

[20] F. B. Mancoff and S. E. Russek, IEEE Trans. Magn. **38**, 2853 (2002).

[21] K. J. Lee, Y. Liu, A. Deac, M. Li, J. W. Chang, S. Liao, K. Ju, O. Redon, J. P. Nozières, and B. Dieny, J. Appl. Phys. **95**, 7423 (2004).

[22] Y. Huai, F. Albert, P. Nguyen, M. Pakala, and T. Valet, Appl. Phys. Lett. **84**, 3118 (2004).

[23] G. D. Fuchs, N. C. Emley, I. N. Krivorotov, P. M. Braganca, E. M. Ryan, S. I. Kiselev, J. C. Sankey, D. C. Ralph, R. A. Buhrman, and J. A. Katine, Appl. Phys. Lett. **85**, 1205 (2004).

[24] S. Kaka, M. R. Pufall, W. H. Rippard, T. J. Silva, S. E. Russek, and J. A. Katine, Nature (London) **437**, 4 (2005).

[25] M. R. Pufall, W. H. Rippard, M. L. Schneider, and S. E. Russek, Phys. Rev. B **75**, 140404(R) (2007).

[26] Q. Mistral, M. van Kampen, G. Hrkac, J.-V. Kim, T. Devolder, P. Crozat, C. Chappert, L. Lagae, and T. Schrefl, Phys. Rev. Lett. **100**, 257201 (2008).

[27] T. Devolder, J.-V. Kim, P. Crozat, C. Chappert, M. Manfrini, M. van Kampen, W. Van Roy, L. Lagae, G. Hrkac, and T. Schrefl, Appl. Phys. Lett. **95**, 012507 (2009).

[28] M. Kuepferling, C. Serpico, M. Pufall, W. Rippard, T. M. Wallis, A. Imtiaz, P. Krivosik, M. Pasquale, and P. Kabos, Appl. Phys. Lett. **96**, 252507 (2010).

[29] S. M. Mohseni, S. R. Sani, J. Persson, T. N. Anh Nguyen, S. Chung, Y. Pogoryelov, and J. Åkerman, Phys. Status Solidi RRL **5**, 432 (2011).

[30] S. R. Sani, J. Persson, S. M. Mohseni, V. Fallahi, and J. Kerman, J. Appl. Phys. **109**, 2009 (2011).

[31] H. Maehara, H. Kubota, Y. Suzuki, T. Seki, K. Nishimura, Y. Nagamine, K. Tsunekawa, A. Fukushima, H. Arai, T. Taniguchi, H. Imamura, K. Ando, and S. Yuasa, Appl. Phys. Express **7**, 023003 (2014).

[32] V. S. Pribiag, I. N. Krivorotov, G. D. Fuchs, P. M. Braganca, O. Ozatay, J. C. Sankey, D. C. Ralph, and R. A. Buhrman, Nat. Phys. **3**, 498 (2007).

[33] S. R. Sani, P. Dürrenfeld, S. M. Mohseni, S. Chung, and J. Åkerman, IEEE Trans. Magn. **49**, 4331 (2013).

[34] T. Silva and W. Rippard, J. Magn. Magn. Mater. **320**, 1260 (2008).

[35] A. Ruotolo, V. Cros, B. Georges, A. Dussaux, J. Grollier, C. Deranlot, R. Guillemet, K. Bouzehouane, S. Fusil, and A. Fert, Nat. Nanotechnol. **4**, 528 (2009).

[36] N. Locatelli, V. V. Naletov, J. Grollier, G. de Loubens, V. Cros, C. Deranlot, C. Ulysse, G. Faini, O. Klein, and A. Fert, Appl. Phys. Lett. **98**, 062501 (2011).

[37] A. D. Belanovsky, N. Locatelli, P. N. Skirdkov, F. Abreu Araujo, J. Grollier, K. A. Zvezdin, V. Cros, and A. K. Zvezdin, Phys. Rev. B **85**, 100409(R) (2012).

[38] Q. Zhu, Q. Zheng, X. Liu, J. Wang, and Q. Liu, J. Appl. Phys. **117**, 173907 (2015).

[39] M. Kreissig, R. Lebrun, F. Protze, K. J. Merazzo, J. Hem, L. Vila, R. Ferreira, M. C. Cyrille, F. Ellinger, V. Cros, U. Ebels, and P. Bortolotti, AIP Adv. **7**, 056653 (2017).

[40] W. K. Hiebert, A. Stankiewicz, and M. R. Freeman, Phys. Rev. Lett. **79**, 1134 (1997).

[41] P. S. Keatley, S. Sani, G. Hrkac, S. Mohseni, P. Drrenfeld, J. Åkerman, and R. Hicken, in *2015 IEEE Magnetics Conference (INTERMAG)* (IEEE, Piscataway, NJ, 2015), pp. 1–1.

[42] P. S. Keatley, S. R. Sani, G. Hrkac, S. M. Mohseni, P. Dürrenfeld, T. H. J. Loughran, J. Åkerman, and R. J. Hicken, Phys. Rev. B **94**, 060402(R) (2016).

[43] P. S. Keatley, S. R. Sani, G. Hrkac, S. M. Mohseni, P. Dürrenfeld, J. Åkerman, and R. J. Hicken, Phys. Rev. B **94**, 094404 (2016).

[44] P. S. Keatley, P. Gangmei, M. Dvornik, R. J. Hicken, J. Grollier, C. Ulysse, J. R. Childress, and J. A. Katine, in *Magnonics: From Fundamentals to Applications*, edited by S. O. Demokritov and A. N. Slavin (Springer, Berlin, 2013), pp. 17–28.

[45] J. TrägÅrdh, K. Macrae, C. Travis, R. Amor, G. Norris, S. H. Wilson, G.-L. Oppo, and G. Mcconnell, J. Microsc. (Oxford, UK) **259**, 66 (2015).

[46] P. S. Keatley, S. R. Sani, G. Hrkac, S. M. Mohseni, P. Dürrenfeld, J. Åkerman, and R. J. Hicken, J. Phys. D **50**, 164003 (2017).

[47] O. V. Sukhostavets, B. Pigeau, S. Sangiao, G. de Loubens, V. V. Naletov, O. Klein, K. Mitsuzuka, S. Andrieu, F. Montaigne, and K. Y. Guslienko, Phys. Rev. Lett. **111**, 247601 (2013).

[48] G. Hrkac, P. S. Keatley, M. T. Bryan, and K. Butler, J. Phys. D **48**, 453001 (2015).

[49] G. Hrkac, D. Hahn, L. Saharan, T. Schrefl, J. V. Kim, T. Devolder, and C. Chappert, IEEE Trans. Magn. **48**, 3811 (2012).

[50] See Supplemental Material at http://link.aps.org/supplemental/10.1103/PhysRevB.100.134439 for all data relevant to all devices presented in this work .

[51] S. Petit-Watelot, J.-V. Kim, A. Ruotolo, R. M. Otxoa, K. Bouzehouane, J. Grollier, A. Vansteenkiste, B. Van De Wiele, V. Cros, and T. Devolder, Nat. Phys. **8**, 682 (2012).

[52] P. S. Keatley, P. Gangmei, M. Dvornik, R. J. Hicken, J. Grollier, and C. Ulysse, Phys. Rev. Lett. **110**, 187202 (2013).